

Full Length Article

DFT and Thermodynamics Calculations of Surface Cation Release in LiCoO_2

Ali Abbaspour-Tamijani, Joseph W. Bennett, Diamond T. Jones, Natalia Cartagena-Gonzalez, Zachary R. Jones, Elizabeth D. Laudadio, Robert J. Hamers, Juan A. Santana, Sara E. Mason

PII: S0169-4332(20)30621-8

DOI: <https://doi.org/10.1016/j.apsusc.2020.145865>

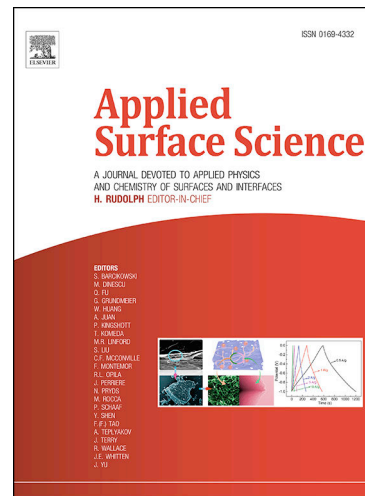
Reference: APSUSC 145865

To appear in: *Applied Surface Science*

Received Date: 31 August 2019

Revised Date: 13 February 2020

Accepted Date: 22 February 2020



Please cite this article as: A. Abbaspour-Tamijani, J.W. Bennett, D.T. Jones, N. Cartagena-Gonzalez, Z.R. Jones, E.D. Laudadio, R.J. Hamers, J.A. Santana, S.E. Mason, DFT and Thermodynamics Calculations of Surface Cation Release in LiCoO_2 , *Applied Surface Science* (2020), doi: <https://doi.org/10.1016/j.apsusc.2020.145865>

This is a PDF file of an article that has undergone enhancements after acceptance, such as the addition of a cover page and metadata, and formatting for readability, but it is not yet the definitive version of record. This version will undergo additional copyediting, typesetting and review before it is published in its final form, but we are providing this version to give early visibility of the article. Please note that, during the production process, errors may be discovered which could affect the content, and all legal disclaimers that apply to the journal pertain.

DFT and Thermodynamics Calculations of Surface Cation Release in LiCoO₂

Ali Abbaspour-Tamijani^{a,1}, Joseph W. Bennett^{a,1}, Diamond T. Jones^a,
 Natalia Cartagena-Gonzalez^c, Zachary R. Jones^b, Elizabeth D. Laudadio^b,
 Robert J. Hamers^b, Juan A. Santana^c, Sara E. Mason^{a,*}

^aDepartment of Chemistry, University of Iowa, Iowa City, Iowa 52242

^bDepartment of Chemistry, University of Wisconsin-Madison, Madison, WI 53706

^cDepartment of Chemistry, The University of Puerto Rico at Cayey, P. O. Box 372230, Cayey, PR 00737-2230, USA

Abstract

While complex metal oxides (CMOs) such as LiCoO₂ (LCO) are currently used in multiple electronic devices, their environmental impacts are not well understood. In this work, we apply density functional theory (DFT) and thermodynamics modeling to study LCO surface transformations. We performed Raman studies on bulk LCO, and compared experimental and computational results. Full vibrational analysis of the model LCO surfaces show localized surface modes that are distinct from bulk, varying in Li and OH surface terminations. Central to this study are calculations to assess the dependence of the DFT + thermodynamics methodology on computational parameters, such as the choice of the exchange-correlation functional, and model geometry, specifically varying slab thickness and supercell dimensions. We discuss how the results can be used to establish upper- and lower-bounds for favorable surface cation vacancy formation under varying pH conditions. The model predicts that at a pH of 7, up to 16% of surface Co will undergo dissolution. We go on to discuss how these model results relate to experimental dissolution studies. We also extrapolate how our results can provide useful insights to guide the (re)design of CMOs with tailored ion release behavior.

Keywords: complex metal oxides, DFT, ion release, dissolution, li-ion battery, environmental chemistry

*Corresponding author

Email addresses: sara-mason@uiowa.edu (Sara E. Mason), sara-mason@uiowa.edu (Sara E. Mason), sara-mason@uiowa.edu (Sara E. Mason), sara-mason@uiowa.edu (Sara E. Mason)

¹These authors contributed equally to this work.

1. Introduction

The production and widespread use of nanoscale complex metal oxides (CMOs) has been a driving force in the global economy [1], specifically in the energy sector where Li-ion batteries [2–6] are the bedrock of portable electronics [7, 8]. The prototypical electroactive CMO used in Li-ion batteries is LiCoO_2 (LCO), with production and use projected to increase [9]. With no established economic incentive to recycle LCO-based batteries, [10], and complications such as compositional and structural variety of the cathodes further hindering recycling strategies, [11] LCO and related complex metal oxides used as cathodes can contribute to electronic waste in landfills [12]. When exposed to different environmental conditions, CMO nanomaterials undergo transformations that are only beginning to be explored, [13–17] and which could have as-yet unknown biological impacts [18–20]. Therefore, molecular-level understanding of how CMOs transform outside of their operational settings and under variable environmental conditions is critical. Furthermore, such information could be used to inform environmental release and fate models, [21–23] and to guide the design of environmentally benign nanomaterials. Such a scheme was recently applied in the case of binary metal oxide materials [24, 25], where high-throughput experimental works were used to inform hazard and risk profiles.

Recent experiments have demonstrated that CMOs such as LCO and $\text{Li}_x(\text{Ni}_y\text{Mn}_z\text{Co}_{1-y-z})\text{O}_2$ (NMC) [17] will partially dissolve in aqueous media, releasing transition metals such as Co^{2+} and Ni^{2+} to solution. The metals released from these CMOs have shown toxicity effects in *Shewanella oneidensis* MR-1 bacteria [9, 16], the eukaryotic water flea *Daphnia magna* [26], and have also been shown to potentially impact the lipid ordering in model cell membranes [27, 28]. The mechanism and driving forces for cation release have been modeled using density functional theory (DFT) calculations coupled with thermodynamics modeling, [14] which captured incongruent release trends observed experimentally. However, calibrating the DFT + thermodynamics modeling using the NMC system is complicated in that the relative amounts of transition metals can vary in different formulations [15, 29]. It is therefore useful to consider experimental information about LCO dissolution, which has been more broadly studied, to further refine and validate the model.

Niemuth *et al.* [30] reports, based on inductively coupled plasma mass spectroscopy (ICP-MS) experiments, that release of Co^{2+} from LCO scales in a logarithmic fashion with time, and that release levels off after long (7 day) exposure times. This suggests a threshold amount of Co^{2+} release occurs in the material, as opposed to continual degradation of LCO in water. In other work, Melby *et al.* [31] report that dissolution of LCO is initialized by fast release of Li^+ , followed by the release of Co^{2+} . This is in-line with previous theoretical studies which suggest that the LCO surface is hydroxylated, and not Li-terminated, under ambient aqueous conditions [13]. Additional experimental studies of Co^{2+} release from LCO go on to consider factors such as surface functionalization [27] and the role of cobalt redox between the solid and aqueous phases [26].

Building upon previous theoretical work of LCO surface stability [13, 32–34], here we apply DFT + thermodynamics modeling to study cation release from the surface in aqueous environments. This comes after our studies of metal release from NMC and its compositionally tuned variants [14, 29]. By focusing on the parent LCO material, we are able to assess model accuracy and go on to outline a general procedure to estimate the amount of surface metal that could dissolve from CMOs as a function of pH. The model development presented here establishes computationally-driven methods for predicting transformations of complex metal oxides in aqueous (environmental) settings. This provides a basis for rational design of cathode materials with tailored dissolution profiles as a means for reducing the negative biological impact of these technologically relevant materials. Theoretical studies using this approach are underway [35]. Many of the surface properties calculated lack a direct experimental comparison. Therefore, we perform and report on benchmarking studies in which computational and model parameters are varied [36]. We also report Raman spectroscopy measurements of bulk LCO, and compare the results to the calculated spectrum. It is well-recognized that the surface -OH functional groups of oxides exhibit vibrational models in the region of 2500–3700 cm⁻¹, and this relatively large range can be attributed to details of the oxygen functional group coordination and chemical environment. For example, for the α -Al₂O₃(0001) surface, the hydroxylated termination exhibits a frequency range of 3600–3750 cm⁻¹, with -OH motions at the lower and higher limits assigned to in-plane and out-of-plane surface -OH groups, respectively [37]. In the case of the anatase TiO₂(101) surface, a hydrated termination shows a broad peak occurring within 2500–3700 cm⁻¹ [38]. Given that there is a wide range of vibrational frequencies reported for oxide surface -OH modes, there is value in calculating detailed vibrational analysis that can inform experiments. In going from the bulk to the surface, we identify surface-localized vibrational modes that differ from bulk modes, and which are also distinct between Li and OH terminated LCO surfaces.

2. Materials and Methods

2.1. Raman Spectroscopy

Raman studies were performed on commercial LiCoO₂ powder (MTI Corporation) on MgO substrates (MTI Corporation). Spectra were collected using a Thermo Fisher Scientific DXR Raman microscope using 532 nm excitation through a 10 \times objective. A full range grating (900 lines/mm) and a 25 μ m slit width resulted in \approx 2 cm⁻¹ resolution. Spectra were adjusted to an atmospheric N₂ line at 2330 cm⁻¹.

2.2. DFT Calculations

DFT calculations were performed with Quantum Espresso [39] unless otherwise stated, using ultrasoft GBRV-type pseudopotentials [40, 41]. Unless otherwise stated, calculations were carried out at the GGA-PBE + U level [42–48] with a Hubbard U value of 5.0 eV for the d -orbitals in Co. A plane-wave cutoff

of 40 Ry was used for the wavefunction, and 320 Ry for the charge density. During structural optimizations, all atoms were allowed to relax until forces were converged to less than 5 meV/Å. Calculations of vibrational modes were carried out by finite displacement methods with the Phonopy package [49], using a displacement of 0.01 Å. Bulk calculations are carried out using a $\sqrt{3} \times \sqrt{3}R30^\circ$ unit cell, for which the total energy is converged using a $6 \times 6 \times 2$ k -grid, and a 1×1 unit cell, for which the total energies converged using an $8 \times 8 \times 8$ k -grid.

We also performed DFT calculations with Projector Augmented Wave (PAW) potentials [50] as implemented in Vienna Ab-initio Simulation Package (VASP) [51]. As DFT fails to fully capture long-range effects [52, 53], we tested the meta-GGA functional, SCAN [54], as well as a van der Waals-corrected one; vdW-BEEF [55]. A wavefunction cutoff energy of 550 eV was used for calculations with PAW potentials. We focus on the SCAN and vdW-BEEF methods because they have been recently suggested as optimal alternatives to GGA + U for various types of materials [56, 57].

2.3. DFT + Thermodynamics Modeling

To study ion release from the LCO surface, DFT + thermodynamics modeling was used as in our previous work [14, 29]. In this method, the Gibbs free energy of ion release, ΔG , is modeled step-wise using both computational and experimental information. The partitioning of elementary reactions is done such that the first term, ΔG_1 , is based entirely on DFT calculations, including zero-point energy corrections to the DFT energy [13]. The chemical equations for the ΔG_1 are presented in detail in the section 3.3 Co Release from $\text{LiCoO}_2(001)$. Following Rong and Kolpak [58], the second term is defined as: $\Delta G_2 = \Delta G_{\text{SHE}}^0 - n_e e U_{\text{SHE}} - 2.303 n_{\text{H}^+} kT \text{pH} + kT \ln a(\text{H}_x \text{AO}_y)^{z^-}$, where ΔG_{SHE}^0 is the free energy of formation at standard state relative to the standard hydrogen electrode (SHE), $e U_{\text{SHE}}$ is the applied potential relative to SHE, and $a_{\text{H}_x \text{AO}_y}^{z^-}$ is the concentration of the dissolved constituent ions (assumed to be 1×10^{-6} M, from previous experiments [9, 16]). n_e and n_{H^+} are the number of electrons and protons, respectively. At conditions of $U_{\text{SHE}}=0$, ΔG can be computed under variable pH values to simulate environmentally relevant dissolution conditions. Based on Pourbaix diagrams [59], $\text{Co}_{(\text{aq})}^{2+}$ is the dominant aqueous speciation of cobalt up until pH = 7. At pH > 7, $\text{HCoO}_{2(\text{aq})}^{-1}$ becomes the preferred speciation, and computed values of ΔG would be shifted to reflect the change in speciation, as discussed previously.[14].

3. Results and Discussion

3.1. Characterization of Bulk LiCoO_2

Figure 1 depicts a top view of bulk LCO (left-hand side), and a side view of the layered structure (right-hand side). Co resides in the center of an oxygen octahedra, and each octahedral unit is edge-sharing, forming a rigid O-Co-O network of height $d1$. Li is found in the space between O-Co-O units, which is of height $d2$. LCO belongs to the Delafossite structure type, so the overall

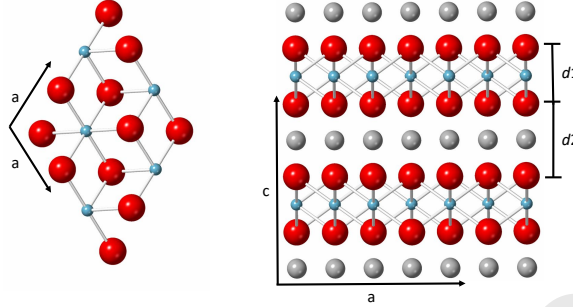


Figure 1: (Left) Top view of a transition metal oxide layer of the $\sqrt{3} \times \sqrt{3}R30^\circ$ bulk LCO cell. (Right) Side view of the layer ordering in LCO, with layer spacings d_1 (O-Co-O) and d_2 (O-Li-O). Co is depicted as cyan, Li is gray and O is red.

Table 1: Lattice parameters (Å) and band gap energy, E_{gap} (eV), calculated with various DFT methods for bulk LCO. Experimental lattice parameters [60] and E_{gap} values [60–63] are also included.

DFTs	a	c	d_1	d_2	E_{gap}
GBRV-PBE+U5	2.843	14.120	2.065	2.643	2.59
PAW-PBE	2.847	14.009	2.029	2.640	1.02
PAW-PBE+U3.3	2.834	14.117	2.055	2.651	2.27
PAW-PBE+U5	2.828	14.177	2.073	2.653	2.84
PAW-SCAN	2.807	13.976	2.044	2.615	2.25
PAW-vdW-BEEF	2.858	14.017	2.061	2.612	1.16
Experiments	2.815	14.049	2.049	2.634	2.5–2.7

crystal symmetry of the system is $R\bar{3}m$ (space group 166). In this structure, the Wyckoff positions are as follows: Li is at 3a, Co is 3b, and O is at 6c, with $u_O = 0.260$.

In Table 1 we report the lattice constants of bulk LCO, calculated with various DFT methods alongside experimental values. The DFT methods yield lattice constant values within 1.6 % of experimental values. As expected, as the applied U value is increased from 3.3 to 5.0 eV, there are increases in the inter-layer spacings and the c lattice constant. Overall, the SCAN functional results in the best agreement with experiment for the a lattice constant, which is in line with comparative studies assessing density functional performance in intercalating transition metal oxides [56]. The high accuracy of the SCAN functional for ground-state structures comes from the correct description of medium-range vdW interaction [64]. The most accurate c cell parameter is predicted by vdW-BEEF functional. This is due to the fact that this functional accounts for long-range effects, which play a role in interlayer interactions and distances. This role ultimately manifests in the value of the c lattice constant.

We also included, in Table 1, calculated and measured values of the band gap energy, E_{gap} . The calculated values of E_{gap} for bulk LCO range from 1.02 to 2.8 eV in going from PBE to PBE + U with $U = 5$ eV, in line with previous calculations [56, 65, 66]. Interestingly, vdW-BEEF performs as poorly as PBE for E_{gap} of LCO, suggesting that such a method is unsuitable to study defected CMOs. This is likely because the type of the exchange functional used in the vdW-BEEF method is a revised PBE, which is only one parameter different than the PBE functionals. As such, it still carries the shortfalls of regular PBE functional in predicting E_{gap} . The experimental values for E_{gap} of LCO are 2.1,[61] 2.5[62] and 2.7[60, 63] eV. The SCAN method also performs very well for the band gap of LCO as recently noted. [56] Note that our SCAN result for the band gap of LCO is 2.25 eV, while in Ref. 50 a value of 1.74 eV was reported (see Table 2 in Ref. 50). However, inspection of the projected density of states (PDOS) in Fig. 3 of Ref. 50 reveals that the SCAN band gap for LCO is close to 2.4 eV. In general, calculations for LCO with PAW-PBE and GBRV-PBE yield similar structural and band gap properties.

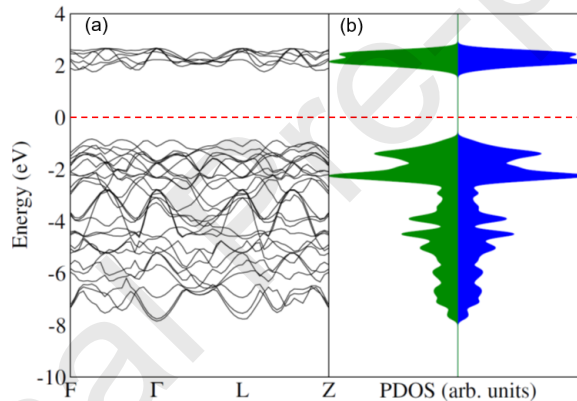


Figure 2: (a) Electronic band structure and (b) PDOS of bulk LCO calculated with the GBRV-PBE+U5 method. Spin-up and spin-down PDOS are shown in blue and green colors, respectively. The Fermi level (E_F) is shown as a dashed line set to $E_F=0$ eV.

DFT calculations were carried out for the electronic structure of the bulk LCO. Projected density of states (PDOS) and electronic band structure is shown in Figure 2. Analysis of the PDOS in Figure 2 shows an equal occupation of spin up and spin down 3d character, with more filled states than empty states; this is consistent with the $3d^6$ occupation formally associated with Co^{3+} . As the calculations with PAW potentials yield a similar electronic structure for bulk LCO, we only report the result from GBRV-PBE calculations, with an applied U value of 5.0 eV, referred to as GBRV-PBE+U5.

To further characterize the bulk structure, we performed an experimental Raman study and a computational vibrational analysis. The Raman spectrum of bulk LCO in the range $400 - 700 \text{ cm}^{-1}$ is shown in Figure 3b. Two major peaks are observed, at 464.8 and 575.7 cm^{-1} . The DFT+ U -calculated frequencies

and normal modes of vibration for LCO are shown in Figure 3a. The doubly degenerate (xy -type) modes are shown on the left, and the singly degenerate (z -type) modes are shown on the right. Based on normal mode analysis, in general, the computed modes can be separated into three frequency regimes. The lower frequency motions are Li-O based motions with some Co displacement mixed in, the middle frequency modes are Co-O based motions with some Li displacement mixed in, and the highest frequency modes are octahedral O_6 cage dilations.

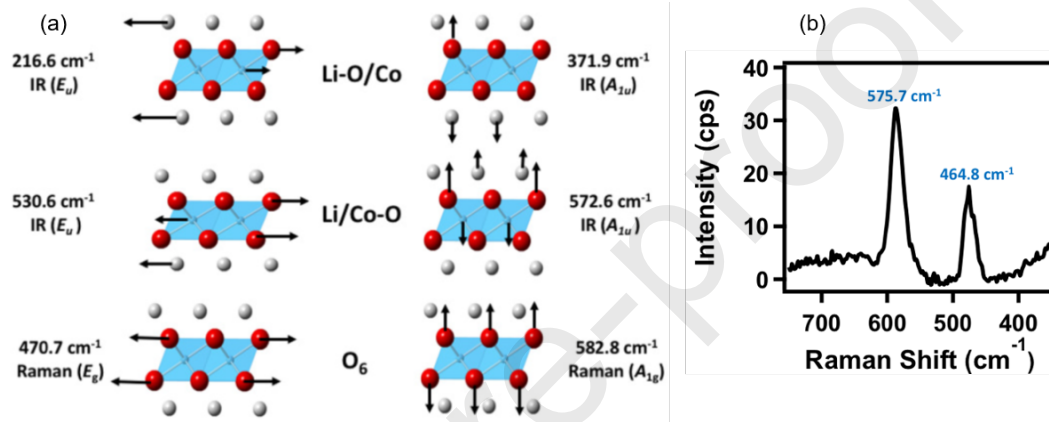


Figure 3: a) GBRV-PBE+U5 calculated vibrational modes and b) experimental Raman Spectra in the range of 400-700 cm^{-1} for bulk LCO.

The irreducible representations of the normal modes of LCO are $\Gamma = A_{1g} + E_g + 2A_{2u} + 2E_u$. The modes can be grouped as either IR ($2A_{2u} + 2E_u$) or Raman ($A_{1g} + E_g$) active. The difference in frequency between the IR active modes in xy (E_u) and z (A_{2u}) for the Li-O/Co and Co-O/Li regimes are ≈ 155 and 42 cm^{-1} , so the two directions should be distinguishable in IR experiments. The Raman active modes from the DFT+ U calculations are 470.7 and 582.8 cm^{-1} , close to the experimental values. The difference in frequency between the Raman active modes in xy (E_u) and z (A_{2u}) for the O_6 cage dilations is $\approx 112.1 \text{ cm}^{-1}$. Our calculated frequencies are in general agreement with a prior study of Li_xCoO_2 , where the amount of Li was varied between $x=0.33$ and 0.87, and significant shifts in the A_{1g} and E_g were observed as the lithiation state was adjusted [67].

3.2. $\text{LiCoO}_2(001)$ Surfaces

Bulk LCO can be cleaved to expose (001), (104), and (110) surfaces [68, 69], with the polar (001) surface being predominant as shown by experiments [9, 16] and DFT calculations [32]. Moreover, first-principles thermodynamics [13] show that the LCO(001) surface exhibits two distinct terminations as a function of chemical environment; *i*) a Li-terminated surface ($\text{LCO}(001)_{\text{h-Li}}$), where Li is above a three-fold hollow surface site (Figure 4a) and *ii*) an OH-terminated

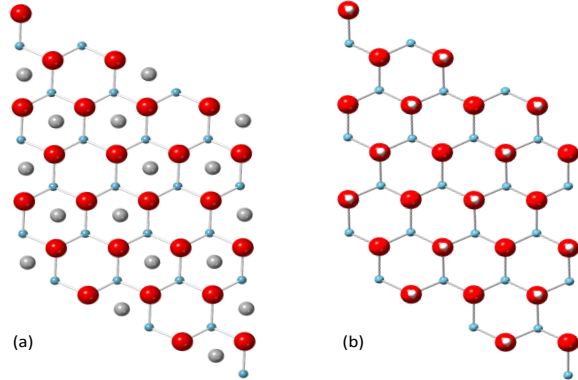


Figure 4: Top down view of the surface layer of LCO for (a) $\text{LCO}_{\text{h-Li}}$ and (b) $\text{LCO}_{\text{h-H}}$. Li is on three-fold hollow surface sites and H is on-top surface oxygen-atoms, forming an O-H bond. The color scheme is the same as Figure 1.

surface ($\text{LCO}(001)_{\text{h-H}}$), where H is directly above an O in the surface layer, forming an OH bond (Figure 4b).

In order to build structural models for the surface, two base unit cells were used. In one set, the surface slabs are based on the primitive hexagonal LCO bulk cell, which we use to create 1×1 , 2×2 , 3×2 , 4×2 , 5×2 , 6×2 , and 4×4 supercells. All surface slabs based on the hexagonal bulk cell include 3 O-Co-O trilayers. The second set of surface models is based on the $\sqrt{3}\times\sqrt{3}R30^\circ$ bulk LCO cell, and include $2\sqrt{3}\times\sqrt{3}$ and $3\sqrt{3}\times\sqrt{3}$ supercells comprised of 4 O-Co-O trilayers. Spanning these different surface models gives us the ability to study different vacancy densities formed upon removal of surface Co. For all supercell calculations, the k -grid is adjusted appropriately, such that the 1×1 , 2×2 , 3×2 , 4×2 , 5×2 , 6×2 , and 4×4 supercells uses k -grids of $8\times 8\times 1$, $4\times 4\times 1$, $3\times 4\times 1$, $2\times 4\times 1$, $2\times 4\times 1$, $2\times 4\times 1$, and $2\times 2\times 1$, respectively. The $2\sqrt{3}\times\sqrt{3}$ and $3\sqrt{3}\times\sqrt{3}$ supercells use k -grids of $3\times 6\times 1$ and $2\times 6\times 1$, respectively.

We discuss our DFT + U results for the electronic and vibrational properties of $\text{LCO}(001)_{\text{h-Li}}$ and $\text{LCO}(001)_{\text{h-H}}$ modeled with (2×2) supercell. The GBRV-PBE-U5 electronic band structure and PDOS of $\text{LCO}(001)_{\text{h-Li}}$ and $\text{LCO}(001)_{\text{h-H}}$ are shown in Figure 5. In Table 2, we include the E_{gap} of $\text{LCO}(001)_{\text{h-Li}}$ and $\text{LCO}(001)_{\text{h-H}}$ calculated with various DFT methods. In general, E_{gap} is similar for $\text{LCO}(001)_{\text{h-Li}}$ and bulk LCO, with some variation between the various DFT methods. The value of E_{gap} is lower for $\text{LCO}(001)_{\text{h-H}}$ than for $\text{LCO}(001)_{\text{h-Li}}$, which results from an increase metallic character due to electron density delocalization on the surface of $\text{LCO}(001)_{\text{h-H}}$ through the network of hydrogen bonding. The two LCO(001) surfaces, as well as bulk LCO, show similar PDOS profiles, pointing towards Co^{3+} as the oxidation state of Co at the surface.

The vibrational modes of the LCO(001) surfaces were calculated for comparison with the bulk vibrational modes. The normal modes of vibration for

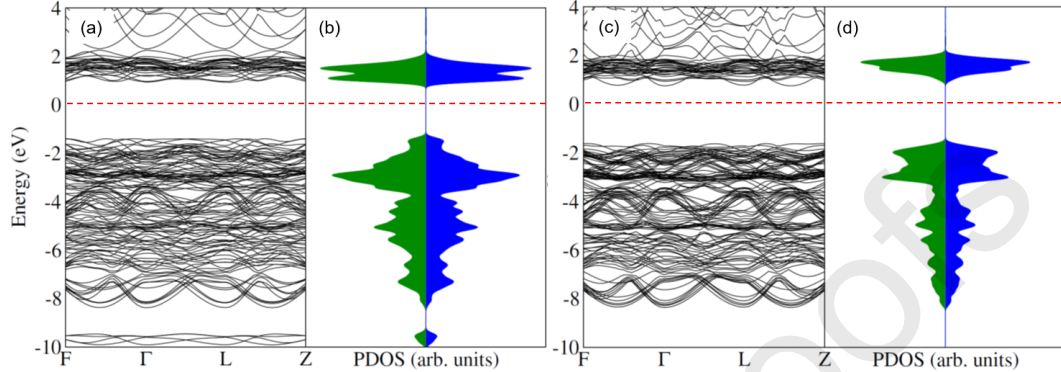


Figure 5: (a,c) Electronic band structure and (b,d) PDOS of (a,b) $\text{LCO}(001)_{\text{h}-\text{H}}$ and (c,d) $\text{LCO}(001)_{\text{h}-\text{Li}}$ calculated at the GBRV-PBE+U5 level. Color scheme is the same as Figure 2.

Table 2: Values of the electronic band gap (eV) calculated with various DFT methods for $\text{LCO}(001)$ and bulk LCO.

DFTs	$\text{LCO}(001)_{\text{h}-\text{Li}}$	$\text{LCO}(001)_{\text{h}-\text{H}}$	bulk LCO
GBRV-DFT+U5	2.37	2.33	2.59
PAW-PBE	1.10	0.87	1.02
PAW-PBE+U3.3	2.28	2.04	2.27
PAW-PBE+U5	2.77	2.57	2.84
PAW-SCAN	2.27	1.97	2.25
PAW-vdW-BEEF	1.06	0.95	1.16

bulk LCO and bulk-like vibrational modes of the two $\text{LCO}(001)$ surface terminations are compared in Table 3. The largest shifts in frequencies are in the Co-O/Li (A_{1u}) and O_6 (A_{1g}) modes in the vertical direction. Relaxation of the two surfaces will change the $d1$ and $d2$ spacings, allowing for larger out of plane distortions than observed in-plane, when compared to the bulk structure. While the bulk-like vibrational modes of the two surfaces are shifted relative to the bulk, they should still be distinguishable.

There are distinct IR-active modes localized to the LCO surface. As shown in Figure 6, the Li and OH-terminated surfaces have surface mode frequencies that are discernible from each other. The surface Li IR active mode is at 386.7 cm^{-1} , and surface OH IR active mode is at 3576.2 cm^{-1} . We note that the Li-terminated surface localized mode is $\approx 15 \text{ cm}^{-1}$ higher in frequency than the corresponding bulk motion and should be differentiable in experiment.

3.3. Co Release from $\text{LiCoO}_2(001)$

The initial dissolution of Co from $\text{LCO}(001)$ is studied with a top-down model of metal release, and follows the preferred mechanism determined from previous work on (isostructural) NMC [14]. To summarize, we assume that the initial state is $\text{LCO}(001)_{\text{h}-\text{Li}}$, and that surface Li exchange with H to create

Table 3: Vibrational frequencies (cm^{-1}) of the bulk-like vibrational modes in $\text{LCO}(001)_{\text{h-Li}}$ (Li-term) and $\text{LCO}(001)_{\text{h-H}}$ (OH-term). The frequency shift (cm^{-1}) of vibrations in the surface relative to bulk LCO are also included.

		bulk	Li-term	shift	OH-term	shift
Li-O/Co	E_u	216.6	213.2	-3.40	207.5	-9.10
Li-O/Co	A_{1u}	371.9	374.2	+2.30	372.0	-0.10
Co-O/Li	E_u	530.6	527.2	-3.40	528.4	-2.20
Co-O/Li	A_{1u}	572.6	555.4	-17.2	572.6	0
O_6	E_g	470.7	459.5	-11.2	462.0	-8.70
O_6	A_{1g}	582.8	594.8	+12.0	603.0	+20.2

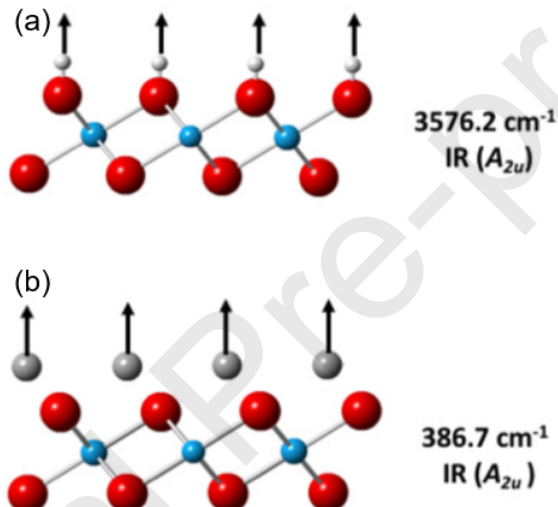


Figure 6: Calculated IR-active surface-localized vibrational modes of the (a) $\text{LCO}(001)_{\text{h-H}}$ and (b) $\text{LCO}(001)_{\text{h-Li}}$ surfaces.

$\text{LCO}(001)_{\text{h-H}}$. An HO-Co unit is then removed from $\text{LCO}(001)_{\text{h-H}}$. The surface exchange reaction is $\text{LCO}(001)_{\text{h-Li}} + x \text{ H} \rightarrow \text{LCO}(001)_{\text{h-H}} + x \text{ Li}$, where dissolution of Li from LCO is an exothermic process. The chemical equation for HO-Co release from $\text{LCO}_{\text{h-H}}$ is: $\text{LCO}(001)_{\text{h-H}} \rightarrow \text{LCO}(001)_{\text{vac}} + \text{Co}_s + \frac{1}{2}\text{H}_{2,g} + \frac{1}{2}\text{O}_{2,g}$, where $\text{LCO}(001)_{\text{vac}}$ represents the slab structure that results from removal of a HO-Co unit from $\text{LCO}_{\text{h-H}}$. In the overall expression for $\Delta G = \Delta G_1 + \Delta G_2$, both the Li-H exchange and the subsequent OH-Co removal contribute to the ΔG_1 term, and each species (Co, H, O, Li) contributes to the ΔG_2 term, where the definition of ΔG_2 follows the details provided in the Materials and Methods, section 2.

ΔG_1 depends on multiple factors, including the details of the DFT calculations, the thickness of LCO(001) slab model, the surface hydroxyl group coverage, and the surface Co-vacancy density. We are able to computationally vary

Table 4: ΔG_1 and ΔG (eV) calculated with various DFT methods for LCO(001).

DFTs	supercell	% H _{surf}	% Co _{vac}	ΔG_1	$\Delta G_{pH=3}$	$\Delta G_{pH=5}$	$\Delta G_{pH=7}$
PAW-PBE	5×2	50	10.00	13.22	-3.61	-3.25	-2.19
PAW-PBE+U3.3	5×2	50	10.00	15.21	-1.62	-1.27	-0.20
PAW-PBE+U5	5×2	50	10.00	14.89	-1.93	-1.58	-0.51
PAW-SCAN	5×2	50	10.00	17.20	0.37	0.73	1.79
PAW-vdW-BEEF	5×2	50	10.00	14.40	-2.43	-2.07	-1.01
GBRV-PBE+U5	5×2	50	10.00	15.46	-1.37	-0.66	0.05
GBRV-PBE+U5	3×2	50	16.67	12.16	1.77	2.25	2.72
GBRV-PBE+U5	2 $\sqrt{3}$ × $\sqrt{3}$	50	16.67	11.49	1.10	1.57	2.04
GBRV-PBE+U5	3 $\sqrt{3}$ × $\sqrt{3}$	55	11.11	14.04	-1.09	-0.38	0.33
GBRV-PBE+U5	3 $\sqrt{3}$ × $\sqrt{3}$	44	11.11	14.89	-0.42	0.17	0.76
GBRV-PBE+U5	3 $\sqrt{3}$ × $\sqrt{3}$	33	11.11	16.71	1.23	1.70	2.17

the Co-vacancy density by using different surface supercells. We performed multiple calculations to isolate and study each of these effects. To explore how values of ΔG_1 depend on the DFT methods, we performed select calculations with GBRV-PBE+U5, PAW-PBE, PAW-PBE+U, PAW-SCAN and PAW-vdW-BEEF. The effects of the number of LCO layers was studied within GBRV-PBE+U5 and using a 2×2 surface model of LCO(001)_{h-H} that included 3 O-Co-O layers and a $2\sqrt{3}\times\sqrt{3}$ surface model, which have an extra interior layer of O-Co-O. The effect of H-coverage in hydrogen-terminated LCO(001) was explored with a $3\sqrt{3}\times\sqrt{3}$ surface model with 55%, 44% and 33% of H-coverage. We performed calculations with 2×2 , 3×2 , 4×2 , 5×2 , 6×2 and 4×4 surface models of LCO(001)_{h-H} to explore Co-vacancy density effects.

In Table 4 we present values of ΔG_1 and ΔG at various pH values and calculated with various DFT methods, using different surface models. By comparing ΔG_1 values for the 5×2 supercell, modeled using variable DFT computational parameters, we can assess how the energies depend on DFT methodology. Comparison shows that ΔG_1 values change by as much as 3.98 eV based on the details of the employed methods. This is not surprising given that ΔG_1 depends on the total energies of LCO slabs, Co_s, Li_s, O_{2,g} and H_{2,g}, and none of the employed DFT methods consistently capture the properties of metallic, semi-conducting and molecular systems. Table 4 also shows how ΔG_1 and ΔG change with the number of LCO layers in the surface model; see GBRV-PBE+U5 calculations with the 3×2 (3 O-Co-O trilayer) and $2\sqrt{3}\times\sqrt{3}$ (4 O-Co-O trilayer) models. ΔG_1 decreases from 12.16 to 11.49 eV in going from 3 O-Co-O trilayers to 4 trilayers. These results reflect that slabs with more atomic layers are more stable, and thus less sensitive to vacancy formation. The results also show that our surface energetics calculated with 3 O-Co-O trilayer surface models of LCO(001) are upper-bounded values. For the $3\sqrt{3}\times\sqrt{3}$ LCO surface, the OH-surface coverage was changed from 5/9 to 4/9 and 3/9 to study how the extent of surface hydroxylation affects Co dissolution. Table 4 shows that for higher OH coverages, Co dissolution is more favorable, and that below a threshold value

Table 5: ΔG_1 and ΔG (eV) calculated with various DFT methods and surface Co-vacancy density for $\text{LCO}(001)_{\text{h}-\text{H}}$.

DFT	supercell	% H _{surf}	% Co _{vac}	ΔG_1	$\Delta G_{\text{pH}=3}$	$\Delta G_{\text{pH}=5}$	$\Delta G_{\text{pH}=7}$
PAW-PBE	2×2	50	25.00	8.23	1.06	1.24	1.77
PAW-PBE	4×2	50	12.50	11.70	-1.91	-1.61	-0.73
PAW-PBE+U3.3	2×2	50	25.00	9.92	2.74	2.92	3.45
PAW-PBE+U3.3	4×2	50	12.50	13.69	0.08	0.37	1.26
PAW-PBE+U5	2×2	50	25.00	9.16	1.98	2.16	2.69
PAW-PBE+U5	4×2	50	12.50	13.12	-0.49	-0.19	0.69
PAW-SCAN	2×2	50	25.00	11.30	4.12	4.30	4.83
PAW-SCAN	4×2	50	12.50	15.44	1.84	2.13	3.02
PAW-vdW-BEEF	2×2	50	25.00	8.72	1.55	1.73	2.26
PAW-vdW-BEEF	4×2	50	12.50	12.65	-0.96	-0.66	0.22
GBRV-PBE+U5	2×2	50	25.00	10.08	2.90	3.26	3.61
GBRV-PBE+U5	4×2	50	12.50	13.93	0.32	0.91	1.50
GBRV-PBE+U5	6×2	50	8.33	17.26	-2.79	-1.96	-1.13
GBRV-PBE+U5	4×4	50	6.25	20.49	-5.59	-4.53	-3.46

of $\approx 40\%$, the process may not occur. The calculations yield insight into how the dissolution process will stop after time, which has been experimentally investigated across a wide range of Li-ion battery cathode material compositions based on LCO and related CMOs [9, 15, 16].

We now turn to discuss the effect of surface Co-vacancy density on ΔG_1 and ΔG . Table 5 shows ΔG_1 and ΔG values for Co vacancy densities ranging from 25% down to 6.25%. We discuss the results in terms of the the extrema. From Table 5, ΔG increases linearly with decreasing % Co vacancy. The linear relationship is driven by the surface exchange reaction $\text{LCO}(001)_{\text{h}-\text{Li}} + x \text{ H} \rightarrow \text{LCO}(001)_{\text{h}-\text{H}} + x \text{ Li}$. By calculating ΔG as a function of pH, we can fit ΔG as a function of pH, and determine the pH value at which $\Delta G=0$. We consider this pH to be the calculated threshold for the onset of surface Co dissolution for a given Co vacancy density. The results of the threshold pH for variable Co vacancy density, calculated with various DFT methods, are plotted in Figure 7. Overall, the calculations suggest that surface Co dissolution beyond 22% may not occur. This is in qualitative agreement with the experimental results reported by Billy et al. for NMC. Based on their account, the leaching efficiency of the Co from NMC fluctuates between 17 and 34% as the pH varies up to 4. Here, the calculated results for LCO at pH 0 predict an upper limit of 22% Co release (Figure 7), and this qualitative agreement suggests that the model results are chemically reasonable.

The model results for Co release also relate to recent studies in which low pH leaching processes were developed to recycle metals from CMOs. Removal of Co from LCO required chelating and reducing agents, such as ascorbic acid and malic acid, to maximize leaching efficiency [70–72]. The trends presented here can also be related to the behavior of small molecule adsorbates such as phos-

phate [73] and carbonate, which have been shown to influence the dissolution of CMOs such as LCO and NMC.

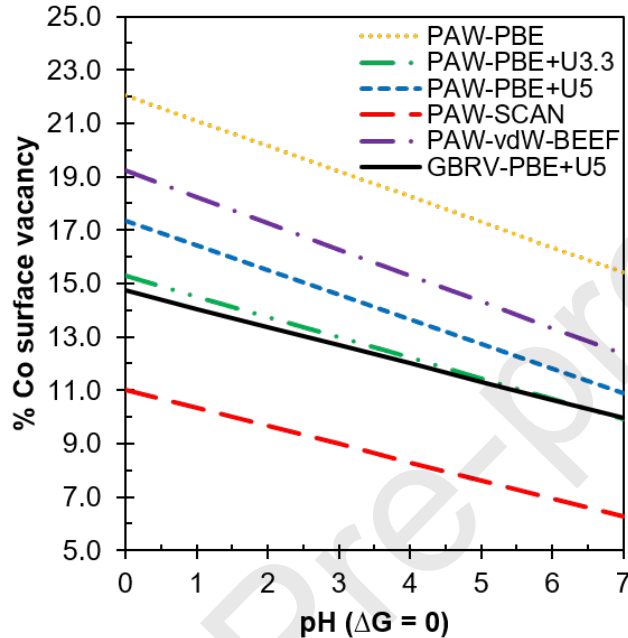


Figure 7: Co surface vacancy density (%) as a function of pH threshold (pH at which $\Delta G=0$), calculated with various DFT methods.

We calculated the electronic band structure of $\text{LCO}(001)_{\text{vac}}$, the defect slab structure that results from Co release. As shown in Figure 8, after removal of a OH-Co surface group, E_{gap} decreases. Furthermore, the PDOS suggests that the oxidation state of surface Co in defected $\text{LCO}(001)$ is Co^{4+} . The change in oxidation state is intuited based on the ideal $3d^5$ configuration of Co^{2+} , which exhibits unequal fillings of spin up and spin down d-states. The change in oxidation state is also consistent with standard operation of Li-ion batteries. The redox active transition metal (Co^{3+}) will respond to changes in the chemical environment (de-lithiation) by oxidizing.

We compare DFT results for the surface Co release in LCO and NMC, which are related by compositional tuning. Calculations with the GBRV-PBE+U5 method shows that Co release from NMC is more favorable than from LCO at similar vacancy densities. For instance, ΔG at $\text{pH} = 3$ and 11.11 % Co vacancy is -0.44 eV in NMC, but predicted to be unfavorable in LCO. This may be explained in part by the differences in structural parameters, such as $d1$ and $d2$, which are 2.07 Å and 2.64 Å for LCO and 2.12 Å and 2.62 Å for NMC [14], respectively. $d1$ is the vertical O-Metal-O distance, and is 0.05 Å larger in NMC than in LCO. This indicates that LCO forms stronger metal oxide bonds

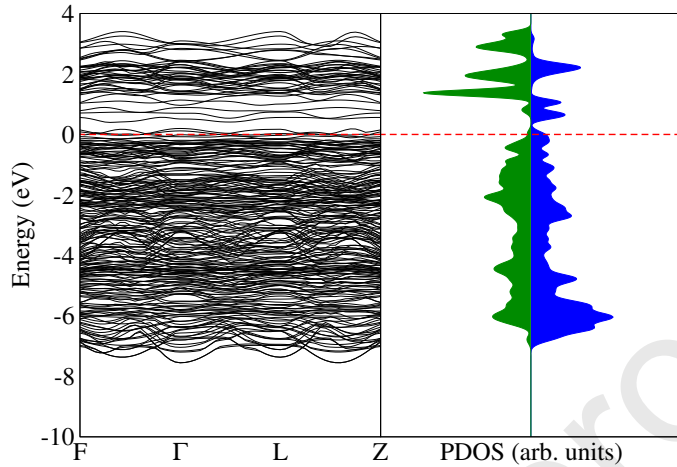


Figure 8: Electronic band structure (left) and PDOS (right) of $\text{LCO}(001)_{\text{vac}}$. Bands crossing E_F have Co 3d character as shown on the right panel.

in the $d1$ layer than NMC. A more significant difference is found in the electronic structure of LCO and NMC; the addition of ferrimagnetic spin-coupling between Ni^{2+} (d^8) and Mn^{4+} (d^3), that results from the different oxidation states of the transition metal will destabilize the lattice relative to LCO, where Co^{3+} has a d^6 electron configuration and no net magnetic moment.

4. Conclusion

In the present work, we used Raman spectroscopy and DFT methods to study the properties of bulk LiCoO_2 . Surface calculations assess how choices in structural models and employed DFT methods affect computed properties. We studied the dissolution process of LCO employing a DFT + thermodynamics approach, spanning different surface supercells, OH coverage, slab thickness, and using different DFT methods. The results show that the DFT + thermodynamics approach can be used to understand the interplay of surface transformations and metal release. The calculated surface Co dissolution energetics depend strongly upon surface area and environmental pH. We found that surface Co vacancy of LCO in water could be at least 7% at pH values close to 7. The model results provide insight about experimental dissolution studies of LCO. For example, Niemuth *et al.* [30] report that dissolution of LCO stops without going to completion. Here, DFT + thermodynamics calculations show that there is a threshold vacancy density (that varies with pH) below which the dissolution process becomes energetically unfavorable. As well, experiments have shown that surface functional groups play a role in the release process. The modeling results indicate an OH mediated release mechanism, supporting the role of surface transformations in the environment on cation release. Significant reactive oxygen species (ROS) generation has been observed alongside

Co²⁺ release [31]. As the details of heterogeneous ROS mechanisms depend on surface functional group identity, this further supports that cation release is mediated and influenced by the type, and density, of surface groups. Collectively, the model results suggest that cation release processes can be controlled through fine-tuning the pH and other external chemical conditions. The ability to model cation release and the early stages of CMO dissolution could provide chemical guidance on future efforts to control release by design, and to inform CMO recycling strategies.

5. Author Information

Corresponding Author: sara-mason@uiowa.edu Notes: The authors declare no competing financial interest.

6. Acknowledgments

This work was supported by National Science Foundation under the Center for Sustainable Nanotechnology, CHE-1503408. The CSN is part of the Centers for Chemical Innovation Program. This research was supported in part through computational resources provided by The University of Iowa, Iowa City, Iowa and the National Science Foundation grant CHE-0840494. This work used the Extreme Science and Engineering Discovery Environment (XSEDE [74]), which is supported by National Science Foundation grant number ACI-1548562. Computational resources were also provided in part by the High-Performance Computing Facility at the University of Puerto Rico, supported by an Institutional Development Award (IDeA) INBRE Grant Number P20GM103475 from the National Institute of General Medical Sciences (NIGMS), a component of the National Institutes of Health (NIH), and the Bioinformatics Research Core of the INBRE. Its contents are solely the responsibility of the authors and do not necessarily represent the official view of NIGMS or NIH. E. D. L. is supported by the National Science Foundation Graduate School and the Office of the Vice Chancellor for Research and Graduate Education at the University of Wisconsin-Madison with funding from the Wisconsin Alumni Research Foundation. The authors thank Dr. Chenyu Wang, and Profs. Christy Haynes, Qiang Cui and Rigoberto Hernandez for useful discussions of this work.

References

- [1] A. A. Keller, S. McFerran, A. Lazareva, and S. Suh. Global Life Cycle Releases of Engineered Nanomaterials. *J. Nanoparticle Res.*, 15:1692, 2013.
- [2] J. B. Goodenough and Y. Kim. Challenges for Rechargeable Li Batteries. *Chem. Mater.*, 2010:587–603, 22.
- [3] B. Dunn, H. Kamath, and J.-M. Tarascon. Electrical Energy Storage for the Grid: A Battery of Choices. *Science*, 334:928–935, 2011.

- [4] N. S. Choi, Z. Chen, S. A. Freunberger, X. Ji, Y. K. Sun, K. Amine, G. Yushin, L. F. Nazar, J. Cho, and P. G. Bruce. Challenges Facing Lithium Batteries and Electrical Double Layer Capacitors. *Angew. Chem. Int. Ed.*, 51:9994–10024, 2012.
- [5] J. B. Goodenough and K.-S. Park. The Li-Ion Rechargeable Battery: A Perspective. *J. Am. Chem. Soc.*, 135:1167–1176, 2013.
- [6] N. Nitta, F. Wu, J.-T. Lee, and G. Yushin. Li-Ion Battery Materials: Present and Future. *Mater. Today*, 18:252–264, 2015.
- [7] J. Lu, Z. Chen, Z. Ma, F. Pan, L. A. Curtiss, and K. Amine. The Role of Nanotechnology in the Development of Battery Materials for Electric Vehicles. *Nature Nanotech.*, 11:1031–1038, 2016.
- [8] L. A.-W. Ellingsen, C. R. Hung, G. Majeau-Bettez, B. Singh, Z. Chen, M. S. Whittingham, and A. H. Stromman. Nanotechnology for Environmentally Sustainable Electromobility. *Nature Nanotech.*, 11:1039–1051, 2016.
- [9] M. N. Hang, I. L. Gunsolus, H. Wayland, E. S. Melby, A. C. Mensch, K. R. Hurley, J. A. Pedersen, C. L. Haynes, and R. J. Hamers. Impact of Nanoscale Lithium Nickel Manganese Cobalt Oxide (NMC) on the Bacterium *Shewanella oneidensis* MR-1. *Chem. Mater.*, pages 1092–1100, 2016.
- [10] J. B. Dunn, L. Gaines, J. C. Kelly, C. James, and K. G. Gallagher. The Significance of Li-Ion Batteries in Electric Vehicle Life-Cycle Energy and Emissions and Recycling's Role in its Reduction. *Energy Environ. Sci.*, 8: 158–168, 2015.
- [11] M. Jacoby. It's Time to get Serious about Recycling Lithium-Ion Batteries. *C&EN*, 97:1–3, 2019.
- [12] K. Zhang, J. L. Schnoor, and E. Y. Zeng. E-Waste Recycling: Where Does It Go from Here? *Environ. Sci. Technol.*, 46:10861–10867, 2012.
- [13] X. Huang, J. W. Bennett, M. N. Hang, E. D. Laudadio, R. J. Hamers, and S. E. Mason. *Ab initio* Atomistic Thermodynamics Study of the (001) Surface of LiCoO₂ in a Water Environment and Implications for Reactivity under Ambient Conditions. *J. Phys. Chem. C*, 121:5069–5080, 2017.
- [14] J. W. Bennett, D. Jones, X. Huang, R. J. Hamers, and S. E. Mason. Dissolution of Complex Metal Oxides from First-Principles and thermodynamics: Cation Removal from the (001) Surface of Li(Ni_{1/3}Mn_{1/3}Co_{1/3})O₂. *Environ. Sci. Technol.*, 52:5792–5802, 2018.
- [15] I. L. Gunsolus, M. N. Hang, N. V. Hudson-Smith, J. T. Buchman, J. W. Bennett, D. Conroy, S. E. Mason, R. J. Hamers, and C. L. Haynes. Influence of Nickel Manganese Cobalt Oxide Nanoparticle Composition on Toxicity toward *Shewanella oneidensis* MR-1: Redesigning for Reduced Biological Impact. *Environ. Sci.: Nano.*, 4:636–646, 2017.

[16] M. N. Hang, N. V. Hudson-Smith, P. L. Clement, Y. Zhang, C. Wang, C. L. Haynes, and R. J. Hamers. Influence of Nanoparticle Morphology on Ion Release and Biological Impact of Nickel Manganese Cobalt Oxide (NMC) Complex Oxide Nanomaterials. *ACS Appl. Nano Mater.*, 1:1721–1730, 2018.

[17] E. Billy, M. Joulie, R. Laucournet, A. Boulineau, E. De Vito, and D. Meyer. Dissolution Mechanisms of $\text{Li}(\text{Ni}_{1/3}\text{Mn}_{1/3}\text{Co}_{1/3})\text{O}_2$ Positive Electrode Material from Lithium-Ion Batteries in Acid Solution. *ACS Appl. Mater. Interfaces*, 10:16424–16435, 2018.

[18] M. A. Maurer-Jones, I. L. Gunsolus, C. J. Murphy, and C. L. Haynes. Toxicity of Engineered Nanoparticles in the Environment. *Anal. Chem.*, 85:3036–3049, 2013.

[19] A. Lopez-Serrano, R. M. Olivas, J. S. Landaluze, and C. Camara. Nanoparticles: A Global Vision. Characterization, Separation, and Quantification Methods. Potential Environmental and Health Impact. *Anal. Chem.*, 6:38–56, 2014.

[20] I. L. Gunsolus and C. L. Haynes. Analytical Aspects of Nanotoxicology. *Anal. Chem.*, 88:451–479, 2016.

[21] F. Gottschalk, T. Sonderer, and R. W. Scholz and B. Nowack. Modeled Environmental Concentrations of Engineered Nanomaterials. *Environ. Sci. Technol.*, 43:9216–9222, 2009.

[22] H. Weinberg, A. Galyean, and M. Leopold. Evaluating Engineered Nanoparticles in Natural Waters. *Trends in Anal. Chem.*, 30:72–83, 2011.

[23] P. Westerhoff and B. Nowack. Searching for Global Descriptors of Engineered Nanomaterial Fate and Transport in the Environment. *Acc. Chem. Res.*, 46:844–853, 2013.

[24] A. Nel and T. Xia and. Nanomaterial Toxicity Testing in the 21st Century: Use of a Predictive Toxicological Approach and High-Throughput Screening. *Acct. Chem. Res.*, 46:607–619, 2013.

[25] C. Kaweeteerawat, A. Ivask, R. Liu, H. Zhang, C. H. Chang, C. Low-Kam, H. Fischer, Z. Ji, S. Pokhrel, Y. Cohen, D. Telesca, J. Zink, L. Madler, P. A. Holden, A. Nel, and H. Godwin. Toxicity of Metal Oxide Nanoparticles in *Escherichia coli* Correlates with Conduction Band and Hydration Energies. *Environ. Sci. Technol.*, 49:1105–1112, 2015.

[26] J. Bozich, M. N. Hang, R. J. Hamers, and R. Klapper. Core Chemistry Influences the Toxicity of Multicomponent Metal Oxide Nanomaterials, Lithium Nickel Manganese Cobalt Oxide and Lithium Cobalt Oxide to *Daphnia Magna*. *Environ. Toxicol. Chem.*, 36:2493–2502, 2017.

- [27] M. Dogangun, M. N. Hang, J. M. Toriano, A. C. McGeachy, E. S. Melby, J. A. Pedersen, R. J. Hamers, and F. M. Geiger. Alteration of Membrane Compositional Asymmetry by LiCoO₂ Nanosheets. *ACS Nano*, 9:8755–8765, 2015.
- [28] M. Dogangun, M. N. Hang, J. Machesky, A. C. McGeachy, N. Dalchand, R. J. Hamers, and F. M. Geiger. Evidence for Considerable Metal Cation Concentrations from Lithium Intercalation Compounds in the Nano-Bio Interface Gap. *J. Phys. Chem. C.*, 121:27473–27482, 2017.
- [29] J. W. Bennett, D. Jones, R. J. Hamers, and S. E. Mason. A First-Principles and Thermodynamics Study of Compositionally-Tuned Complex Metal Oxides: Cation Release from the (001) Surface of Mn-rich Lithium Nickel Cobalt Oxide. *Inorg. Chem.*, 57:13300–13311, 2018.
- [30] N. J. Niemuth, B. J. Curtis, M. N. Hang, M. J. Gallagher, D. H. Fairbrother, R. J. Hamers, and R. D. Klapper. Next-Generation Complex Metal Oxide Nanomaterials Negatively Impact Growth and Development in the Benthic Invertebrate *Chironomus riparius* upon Settling. *Environ. Sci. Technol.*, 53:3860–3870, 2019.
- [31] E. S. Melby, Y. Cui, J. Borgatta, A. C. Mensch, M. N. Hang, W. B. Chrisler, A. Dohnalkova, J. M. Van Gilder, C. M. Alverez, J. N. Smith, R. J. Hamers, and G. Orr. Impact of Lithiated Cobalt Oxide and Phosphate Nanoparticles on Rainbow Trout Gill Epithelial Cells. *Nanotoxicology*, 12:1166–1181, 2018.
- [32] D. Kramer and G. Ceder. Tailoring the Morphology of LiCoO₂: A First Principles Study. *Chem. Mater.*, 21:3799–3809, 2009.
- [33] L. Daheron, H. Martinez, R. Dedryvere, I. Baraille, M. Menetrier, C. Denage, C. Delmas, and D. Gonbeau. Surface Properties of LiCoO₂ Investigated by XPS Analyses and Theoretical Calculations. *J. Phys. Chem. C*, 113:5843–5852, 2009.
- [34] L. Hu, Z. Xiong, C. Ouyang, S. Shi, Y. Ji, M. Lei, Z. Wang, H. Li, X. Huang, and L. Chen. *Ab initio* Studies on the Stability and Electronic Structure of LiCoO₂ (003) Surfaces. *Phys. Rev. B*, 71:125433–1–10, 2005.
- [35] J. W. Bennett, D. T. Jones, B. G. Hudson, J. Melendez-Rivera, R. J. Hamers, and S. E. Mason. First-Principles and Thermodynamics Comparison of Compositionally-Tuned Delafossites: Cation Release from the (001) Surface of Complex Metal Oxides. *Environ. Sci.: Nano*, 11 2019. doi: <https://doi.org/10.26434/chemrxiv.10046276.v1>.
- [36] A. Chakraborty, S. Kunnikuruvan, S. Kumar, B. Markovsky, and D. Aurbach. Layerd Cathode Materials for Lithium-Ion Batteries: Review of Computational Studies on LiNi_{1-x-y}CoxMn_yO₂ and LiNi_{1-x-y}Co_xAl_yO₂. *Chem. Mater.*, 32:915–952, 2020.

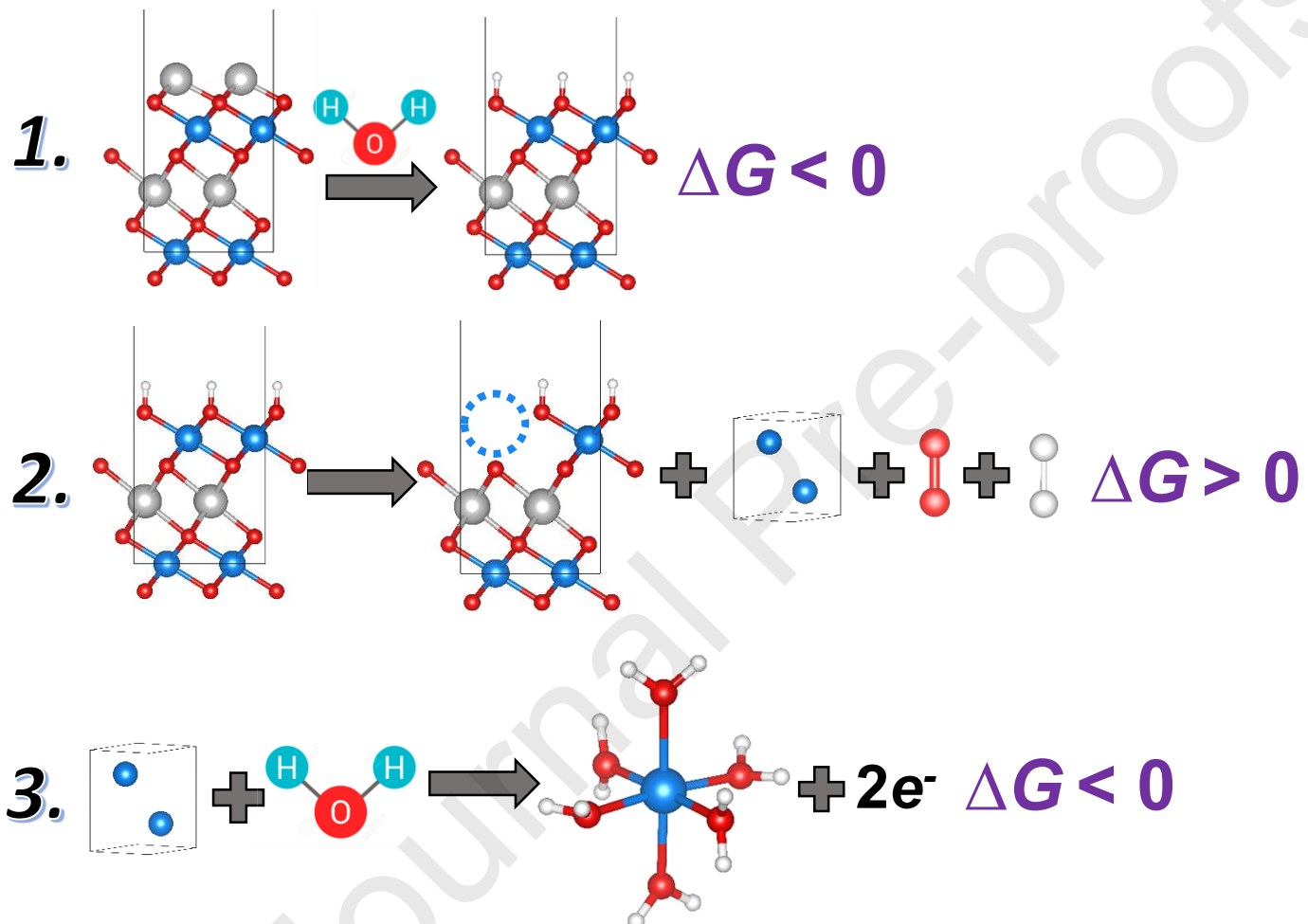
- [37] G. Melani, Y. Nagata, J. Wirth, and P. Saalfrank. Vibrational Spectroscopy of Hydroxylated α -Al₂O₃(0001) Surfaces With and Without Water: An *ab initio* Molecular Dynamics Study. *J. Chem. Phys.*, 149:014707, 2018.
- [38] C. Y. Wu, K. J. Tu, J. P. Deng, Y. S. Lo, and C. H. Wu. Markedly Enhanced Surface Hydroxyl Groups of TiO₂ Nanoparticles with Superior Water-Dispersibility for Photocatalysis. *Materials*, 10:566–581, 2017.
- [39] P. Giannozzi, S. Baroni, N. Bonini, M. Calandra, R. Car, C. Cavazzoni, D. Ceresoli, G. L. Chiarotti, M. Cococcioni, I. Dabo, and et al. Quantum ESPRESSO: A Modular and Open-Source Software Project for Quantum Simulations of Materials. *J. Phys.: Condens. Matter*, 21:395502–20, 2009.
- [40] D. Vanderbilt. Soft Self-Consistent Pseudopotentials in a Generalized Eigenvalue Formalism. *Phys. Rev. B Rapid Comm.*, 41:7892–5, 1990.
- [41] K. F. Garrity, J. W. Bennett, K. M. Rabe, and D. Vanderbilt. Pseudopotentials for High-Throughput DFT Calculations. *Comp. Mater. Sci.*, 81: 446–452, 2014.
- [42] J. Hubbard. Electron Correlation in Narrow Energy Bands. *Proc. R. Soc. Lond. A*, 276:238–257, 1963.
- [43] V. I. Anisimov and O. Gunnarsson. Density Functional Calculation of Effective Coulomb Interactions in Metals. *Phys. Rev. B.*, 43:7570, 1991.
- [44] V. I. Anisimov, F. Aryasetiawan, and A. I. Lichtenstein. First-principles Calculations of the Electronic Structure of Strongly Correlated Systems: the LDA + *U* Method. *J. Phys. Cond. Matter*, 9:767, 1997.
- [45] A. B. Shick, A. I. Liechtenstein, and W. E. Pickett. Implementation of the LDA+*U* Method Using the Full-Potential Linearized Augmented Plane-Wave Basis. *Phys. Rev. B*, 60:10763–9, 1999.
- [46] M. Cococcioni and S. de Gironcoli. Linear Response Approach to the Calculation of the Effective Interaction Parameters in the LDA + *U* Method. *Phys. Rev. B*, 71:035105–1–16, 2005.
- [47] M. Cococcioni. Accurate and Efficient Calculations on Strongly Correlated Minerals with the LDA + *U* Method: Review and Perspectives. *Rev. in Mineral. and Geochem.*, 71:147–167, 2010.
- [48] J. W. Bennett, B. G. Hudson, I. K. Metz, D. Liang, S. Spurgeon, Q. Cui, and S. E. Mason. A Systematic Determination of Hubbard *U* Using the GBRV Ultrasoft Pseudopotential Set. *Comp. Mater. Sci.*, 170:109137–1–10, 2019.
- [49] A. Togo and I. Tanaka. First-Principles Phonon Calculations in Materials Science. *Scripta Materialia*, 108:1–5, 2015.

- [50] G. Kresse and D. Joubert. From Ultrasoft Pseudopotentials to the Projector Augmented-Wave Method. *Phys. Rev. B*, 59:1758–1775, 1999.
- [51] G. Kresse and J. Furthmuller. Efficient iterative schemes for *ab initio* total-energy calculations using a plane-wave basis set. *Phys. Rev. B*, 54:11169–86, 1996.
- [52] M. Aykol, S. Kim, and C. Wolverton. van der Waals Interactions in Layered Lithium Cobalt Oxides. *J. Phys. Chem. C*, 119:19053–19058, 2015.
- [53] A. Abbaspour Tamijani, A. Salam, and M. P. de Lara-Castells. Adsorption of noble-gas atoms on the TiO₂(110) Surface: An *ab initio*-assisted study with van der Waals-Corrected DFT. *J. Phys. Chem. C*, 120:18126–18139, 2016.
- [54] J. Sun, A. Ruzsinsky, and J. P. Perdew. Strongly Constrained and Appropriately Normed Semilocal Density FunctionalStrongly Constrained and Appropriately Normed Semilocal Density Functional. *Phys. Rev. Lett.*, 115: 1–6, 2015.
- [55] J. Wellendorff, K. T. Lundgaard, A. Mogelhøj, V. Petzold, D. D. Landis, J. K. Norskov, T. Bligaard, and K. W. Jacobsen. Density Functionals for Surface Science: Exchange-Correlation Model Development with Bayesian Error Estimation. *Phys. Rev. B*, 85:1–23, 2012.
- [56] A. Chakraborty, M. Dixit, D. Aurbach, and D. T. Major. Predicting Accurate Cathode Properties of Layered Oxide Materials Using the SCAN Meta-GGA Density Functional. *npj Computat. Mater.*, 4:1–9, 2018.
- [57] Y. Zheng, M. Zhang, Q. Li, Y. Zhu, Z. Sui, and D. Chen. Electronic Origin of Oxygen Transport Behavior in La-Based Perovskites: A Density Functional Theory Study. *J. Phys. Chem. C*, 123:275–290, 2019.
- [58] X. Rong and A. M. Kolpak. Ab initio Approach for Prediction of Oxide Surface Structure, Stoichiometry, and Electrocatalytic Activity in Aqueous Solution. *Phys. Chem. Lett.*, 6:1785–1789, 2015.
- [59] K. A. Persson, B. Waldwick, P. Lazic, and G. Ceder. Prediction of Solid-Aqueous Equilibria: Scheme to Combine First-Principles Calculations of Solids with Experimental Aqueous States. *Phys. Rev. B.*, 85:235438, 2012.
- [60] J. van Elp, J. L. Wieland, H. Eskes, P. Kuiper, and G. A. Sawatzky. Electronic structure of CoO, Li-doped CoO, and LiCoO₂. *Phys. Rev. B*, 44: 6090–6103, 1991.
- [61] K. Kushida and K. Kuriyama. Narrowing of the Co-3d band related to the Order–Disorder Phase Transition in LiCoO₂. *Solid State Commun.*, 123: 349–352, 2002.

- [62] J. Rosolen and F. Decker. Photochemical Behavior of LiCoO₂ Membrane Electrode. *Electroanal. Chem.*, 501:253–259, 2001.
- [63] D. Ensling, A. Thissen, S. Laubach, P. C. Schmidt, and W. Jaegermann. Electronic Structure of LiCoO₂ Thin Films: A Combined Photoemission Spectroscopy and Density Functional Theory Study. *Phys. Rev. B*, 82: 195431–1–16, 2010.
- [64] J. H. Yang, D. A. Kitchaev, and G. Ceder. Rationalizing Accurate Structure Prediction in the Meta-GGA SCAN Functional. *Phys. Rev. B*, 100:035132, 2019.
- [65] J. A. Santana, K. Jeongnim, P. R. C. Kent, and F. A. Reboreda. Successes and Failures of Hubbard-Corrected Density Functional Theory: The Case of Mg Doped LiCoO₂. *J. Chem. Phys.*, 141:164706, 2014.
- [66] D. H. Seo, A. Urban, and G. Ceder. Calibrating Transition-Metal Energy Levels and Oxygen Bands in First-Principles Calculations: Accurate Prediction of Redox Potentials and Charge Transfer in Lithium Transition-Metal Oxides. *Phys. Rev. B*, 92:115118, 2015.
- [67] H. L. Liu, T. Y. Ou-Yang, H. H. Tsai, P. A. Lin, H. T. Jeng, G. J. Shu, and F. C. Chou. Electronic Structure and Lattice Dynamics of Li_xCoO₂ Single Crystals. *New J. Phys.*, 17:103004–1–8, 2015.
- [68] Y. Kim, H. Lee, and S. Kang. First-Principles and Experimental Investigation of the Morphology of Layer-Structured LiNiO₂ and LiCoO₂. *J. Mater. Chem.*, 22:12874–12881, 2012.
- [69] T. Ohzuku and A. Ueda. Solid-State Redox Reactions of LiCoO₂ *R*̄₃*m* for 4 Volt Secondary Lithium Cells. *J. Electrochem. Soc.*, 141:2972–2977, 1994.
- [70] L. Li, J. Ge, R. Chen, F. Wu, S. Chen, and X. Zhang. Environmental Friendly Leaching Reagent for Cobalt and Lithium Recovery from Spent Lithium-Ion Batteries. *Waste Management*, 30:2615–2621, 2010.
- [71] G. Zeng, X. Deng, S. Luo, X. Luo, and J. Zou. A Copper-Catalyzed Bioleaching Process for Enhancement of Cobalt Dissolution from Spent Lithium-Ion Batteries. *J. Hazard. Mater.*, 199–200:164–169, 2012.
- [72] L. Li, J. Lu, Y. Ren, X. X. Zhang, R. J. Chen, F. Wu, and K. Amine. Ascorbic-Acid-Assisted Recovery of Cobalt and Lithium from Spent Li-Ion Batteries. *J. Power Sources*, 218:21–27, 2012.
- [73] E. D. Laudadio, J. W. Bennett, S. E. Mason, and R. J. Hamers. Impact of Phosphate Adsorption on Complex Cobalt Oxide Nanoparticle Dispersibility in Aqueous Media. *Environ. Sci. Technol.*, 52:10186–10195, 2018.

[74] J. Towns, T. Cockerill, M. Dahan, I. Foster, K. Gaither, A. Grimshaw, V. Hazlewood, S. Lanthrop, D. Lifka, G. D. Peterson, R. Roskies, J. R. Scott, and N. Wilkins-Diehr. XSEDE:Accelerating Scientific Discovery. *Comp. Sci. Engineering*, 16:62–74, 2014.

- DFT + Thermodynamics to predict cobalt release from oxide surfaces in water
- DFT vibrational analysis of surface termination-specific modes
- Benchmarking provides upper- and lower-bounds for modeled surface properties
- In water, surface Co release from lithium cobalt oxide is at least 7% at neutral pH



Author Contributions

Ali Abbaspour-Tamijani: Conceptualization, Methodology, Analysis, Validation, Writing original draft, Writing review and editing, Investigation and visualization.

Joseph W. Bennett: Conceptualization, Methodology, Analysis, Validation, Writing original draft, Writing review and editing, Investigation and visualization.

Diamond T. Jones: Validation, Formal Analysis, Investigation, Writing- Review and editing

Natalia Cartagena-Gonzalez: Investigation

Zachary R. Jones: Investigation, Writing- Original Draft, Methodology, Validation, and Formal Analysis

Elizabeth D. Laudadio: Investigation, Writing- Original Draft, Validation, and Formal Analysis

Robert J. Hamers: Project Administration and Resources

Juan A. Santana: Project Administration, Supervision, and Investigation

Sara E. Mason: Resources, Funding Acquisition, Project Administration, Supervision, Writing- Review & Editing, and Writing- Original Draft

Declaration of interests

The authors declare that they have no known competing financial interests or personal relationships that could have appeared to influence the work reported in this paper.

The authors declare the following financial interests/personal relationships which may be considered as potential competing interests:

